

Spin-lattice and spin-electronic interactions in the van der Waals semiconductor $\text{Co}_2\text{P}_2\text{S}_6$ Kiri Van Koughnet¹, Ben Mallett^{1,2}, Shen Chong^{1,2}, Benjamin S. Conner^{3,4},
Michael A. McGuire⁶, Michael A. Susner⁵ and Robert G. Buckley^{1,2}¹Robinson Research Institute, Victoria University of Wellington, P.O. Box 33—436, Lower Hutt 5046, New Zealand²MacDiarmid Institute for Advanced Materials and Nanotechnology, P.O. Box 600, Wellington 6140, New Zealand³Sensors Directorate, Air Force Research Laboratory, 2241 Avionics Circle, Wright-Patterson Air Force Base, Ohio 45433, USA⁴National Research Council, 500 Fifth Street NW, Washington, DC 20001, USA⁵Materials and Manufacturing Directorate, Air Force Research Laboratory, 2179 12th Street,
Wright-Patterson Air Force Base, Ohio 45433, USA⁶Materials Science and Technology Division, Oak Ridge National Laboratory, 1 Bethel Valley Road, Oak Ridge, Tennessee 37831, USA (Received 15 December 2023; revised 28 February 2024; accepted 25 March 2024; published 23 April 2024)

We report the results of a temperature-dependent reflection spectroscopy study, across a wide energy range (~ 0.01 to 3 eV), of unsubstituted and 40% Zn substituted for Co, for the transition-metal phosphorus trichalcogenide, $\text{Co}_2\text{P}_2\text{S}_6$. We observe a transition from a paramagnetic to antiferromagnetic state with a Néel temperature at $T_N \sim 120$ K that is completely suppressed in Zn-substituted samples. At 300 K we identify four narrow (~ 1 meV) infrared active phonon modes while at 70 K (below T_N) we observe that the low-energy phonons, dominated by Co motion, resolve into two modes. These low-energy modes are asymmetric, indicating coupling to a broad electronic continuum. We also report a broad (~ 30 meV) low-temperature infrared absorption band that appears near T_N that we suggest is determined by a multiphonon-assisted 2-magnon absorption process. At 300 K in higher-energy spectra, we observe considerable absorption starting from 0.20 ± 0.02 eV which we associate with inter- Co^{2+} ion $3d$ transitions. At temperatures below T_N the number of electronic absorption bands increases from 4 to 6, indicating a lowering of the symmetry around the Co^{2+} ions. On substituting 40% Zn for Co, the antiferromagnetic transition is suppressed along with temperature-dependent changes in the phonon and electronic spectra. The temperature-dependent spectral changes indicate strongly correlated behavior between the infrared active lattice vibrations, the electronic excitations, and magnetism in unsubstituted $\text{Co}_2\text{P}_2\text{S}_6$.

DOI: [10.1103/PhysRevB.109.165142](https://doi.org/10.1103/PhysRevB.109.165142)

I. INTRODUCTION

For many years there has been interest in strongly correlated d -band compounds due to their complex ground state from which a wide range of quantum behaviors arise [1,2]. Recently attention has focused on two-dimensional (2D) correlated electronic systems exhibiting enhanced interactions involving lattice vibrations, spin and orbital magnetism, charge and topological phases, e.g., graphene and transition-metal dichalcogenides [3–7]. Not only are the emerging phenomena of these 2D systems interesting from a fundamental point of view, they also offer opportunities for applications, e.g., electrochemistry, catalysis, hydrogen storage, and spintronics [8–12]. Due to the emerging appreciation of the intriguing physics in low-dimensional systems, renewed interest has been developing in the layered van der Waals transition-metal phosphorus trichalcogenides, TPX_3 , (where T^{2+} is a $3d$ transition metal and X is a chalcogen) [13]. In this series of compounds which fit the formula, $T_2^{2+}[\text{P}_2\text{X}_6]^{4-}$, the chalcogenide atoms form the outer surfaces of a close-packed layer, creating a hexagonal array of octahedral sites accommodating the T^{2+} ions and the P_2 dimers, with 2/3 of the sites occupied by T^{2+} ions and 1/3 of the sites occupied by P_2 dimers, the latter being tetrahedrally bonded to 3 T^{2+} ions and 1 other P atom. The parallel surface planes of chalcogenide atoms are bonded to each other by weak van der Waals forces

exhibiting a stacking sequence of AAA [13–15]. Single-crystal x-ray-diffraction (XRD) refinements show that there are two TPX_3 groups per unit cell, i.e., $T_2\text{P}_2\text{S}_6$ forming a monoclinic structure with a $C2/m$ space group [14]. Many of these compounds can be exfoliated down to a single layer, where it is observed they maintain their correlated 2D magnetic behavior [7,16,17]. Depending on the relative magnitudes of the exchange interactions a range of magnetic ground states are realized. Calculations support the observations, showing that in addition to the nearest-neighbor exchange interaction (J_1), the second- (J_2), and particularly the third- (J_3), nearest-neighbor exchange interactions are critical in determining the magnetic ground state [18,19]. Not unexpectedly, where the T^{2+} ion is a full d shell, such as Zn or Cd, the compounds do not exhibit magnetism.

To understand the structural and electronic behavior of the TPS_3 compounds numerous spectral probes were applied in the 1980–90s to understand their potential use as intercalation compounds in Li-ion batteries and as catalysts [20]. Infrared (IR) investigations were undertaken at ambient temperature on a range of compositions with the assignment of the main vibrational modes and understood in terms of normal modes of the $[\text{P}_2\text{X}_6]^{4-}$ units and the transition-metal ion [21–24]. Probing the impact of magnetism on the IR-active modes was explored by measuring absorption at 5 K on TPX_3 ($T = \text{Fe}, \text{Ni}$ and $X = \text{S}, \text{Se}$) showing an increase in

the number of modes that was interpreted as phonon folding in the antiferromagnetic phase [25]. A similar study of TPX_3 ($T = \text{Mn, Fe, Ni}$ and $X = \text{S, Se}$) did not exhibit any temperature dependence down to 120 K except for FePS_3 [26]. Measurements on CdPS_3 down to 100 K did not, as expected given the full d shell, show any temperature dependence [21]. Depending on the polarization, Raman studies demonstrated an increase in the number of low-energy modes below T_N [21,27–29]. Liu and co-workers also report scattering off 2 magnons in $\text{Co}_2\text{P}_2\text{S}_6$, the presence of which is indicated in neutron-scattering measurements [30]. Lattice dynamics calculations show as expected in these 2D materials, bands exhibiting little dispersion with a gap between the low-energy metal-dominated vibrations and the higher-energy $[\text{P}_2\text{X}_6]^{4-}$ stretching modes [24,31–33].

High-energy reflectance studies out to 30 eV have been undertaken on TPS_3 where $T = \text{Fe, Ni, Zn}$ with remarkably similar spectra, suggesting that in this energy range the response is dominated by transitions involving the $[\text{P}_2\text{X}_6]^{4-}$ ion and that the d states do not contribute [34–36]. At lower energies (1–6 eV) TPS_3 compounds exhibit a series of absorption bands that are understood in terms of intra- and inter- d -state transitions [3,37–42]. Electronic band-structure calculations, using different approaches, have been reported that are consistent with the optical studies above ~ 0.1 eV [33,43–48]. These band-structure calculations on NiPS_3 indicate that within 20 eV of the Fermi level the valence band comprises S-3 p , S-3 s , P-3 s , and Ni-3 d states. Within 10 eV of the Fermi level the conduction band comprises S-3 p , P-3 s , and -3 p , and Ni-4 s and 4 p states [44]. The lowest-energy electronic absorption edge in the TPS_3 materials is determined by transitions between the partially filled d shell of the transition ions. For the Mn, Fe, Co, and Ni compounds, the transition metal is in an octahedral crystal field, which splits the d levels, thus determining not only the magnetic ground state, but also the electronic behavior including the lowest-energy optical gap [7,47]. Distortions of the octahedral crystal field and exchange interactions will further split the d levels [39,46]. For compositions with filled d bands, such as ZnPS_3 , the d states lie well removed from the Fermi level. So, unlike compositions with a partially filled d shell, ZnPS_3 is nonmagnetic and exhibits a significant energy gap with the electronic absorption edge being determined by transitions between S-3 p and Zn-4 s states [45].

Due to difficulties in preparing high-quality crystals, $\text{Co}_2\text{P}_2\text{S}_6$ has not been as extensively studied as some of the other TPS_3 compounds. Nonetheless neutron-scattering studies have confirmed the atomic structure and observed a commensurate magnetic structure of high-spin Co^{2+} ions forming a 2D antiferromagnetic honeycomb lattice with an antiferromagnetic alignment along the a axis, a ferromagnetic alignment along the b axis, and a small out-of-plane component along the c axis [49]. The Néel temperature, T_N , was measured to be 119.1 ± 0.1 K [49]. Depending on polarization, the low-energy Co^{2+} Raman-active modes resolve into two modes below T_N which are accompanied by a rising broad background signal that has been interpreted as due to 2-magnon scattering. Interestingly the neutron scattering also indicates spin fluctuations exist above T_N [50], behavior also observed in MnPS_3 [51].

In this paper we report a reflection spectroscopy study of the antiferromagnet $\text{Co}_2\text{P}_2\text{S}_6$ crystals over an extended spectral range (~ 0.01 to ~ 3 eV) probing both the lattice vibrations and the near-Fermi energy electronic transitions. We also present results for a 40% Zn substitute crystal where the long-range antiferromagnetism has been suppressed. By comparing spectral measurements on $\text{Co}_2\text{P}_2\text{S}_6$ and 40% Zn-substituted crystals, above and below T_N , we observe significant changes in both the electronic and vibrational spectra for unsubstituted $\text{Co}_2\text{P}_2\text{S}_6$, changes that are not observed in the 40% Zn-substituted crystal. We thereby demonstrate the strongly correlated behavior between the IR-active lattice vibrations, the electronic excitations, and magnetism in $\text{Co}_2\text{P}_2\text{S}_6$.

II. EXPERIMENT

We synthesized single crystals of $\text{Co}_2\text{P}_2\text{S}_6$ using the general procedures outlined in Refs. [13,49,52]. We combined Co powder (Alfa Aesar Puratronic, 22 mesh, 99.998%, reduced), P chunks (Alfa Aesar Puratronic, 99.999%), and S (Alfa Aesar Puratronic, 99.9995%) under vacuum in a sealed quartz ampoule using a near-stoichiometric ratio (i.e., slight excess of P) to form $\text{Co}_2\text{P}_2\text{S}_6$ together with an appropriate quantity (~ 100 mg) of I_2 as the vapor transport agent. We then increased the ampoule temperature over 30 h to the reaction temperature of 650°C , held it there for 4 days, and cooled over a period of 30 h to room temperature. Typical crystals were 4–6 mm in size along the a - b planes with several exceeding 12 mm. Typical thicknesses were < 0.5 mm. The compositions of the samples were determined through subjecting at least three distinct single-crystal specimens of each batch to electron microscopy–energy-dispersive x-ray spectroscopy (SEM-EDS) analysis (3–4 spots per crystal for 9–12 spots total per batch) using a Thermo Scientific UltraDry EDS spectrometer joined with a JEOL JSM-6060 SEM. Chemical vapor transport growth of TPS_3 alloys is not a particularly well controlled nor understood process with the outcome in our case, that the vapor phase containing Zn is more volatile than the vapor phase containing Co. Thus, the composition of the transported crystals was richer in Zn than the starting material (which was 20%) and exhibited a 16% variation in Zn content. Two compositions were investigated; pure $\text{Co}_2\text{P}_2\text{S}_6$ (EDS composition was stoichiometric at $\text{Co}_{2.04(10)}\text{P}_{2.02(2)}\text{S}_{5.94(8)}$) and crystals with a 40% Zn substitution for Co (the EDS-derived composition was $\text{Co}_{1.23(10)}\text{Zn}_{0.79(13)}\text{P}_{2.02(2)}\text{S}_{5.95(11)}$). As will be discussed below, the latter composition was employed as a benchmark given it suppresses the long-range antiferromagnetic transition. The growth process produced clusters of crystals with their growth habit parallel to the ab plane. They were micaceous and easily cleaved parallel to the ab plane. The relatively thin, easily distorted crystals required changes to our usual approach to making photometrically accurate optical measurements and will be discussed below. Samples with a suitable optical surface were carefully selected with either as-grown surfaces or from exfoliated surfaces. Before measurement, the surface was washed in isopropyl alcohol, a step we found important to get consistent optical results on different crystals.

We collected XRD spectra off a flat crystal face (00 l) using a Philips PANalytical system employing Cu K_{α} x-ray radiation at a wavelength of $\lambda_{K_{\alpha 1}} = 0.154056$ nm. For the variable-temperature studies, we used an Oxford PheniX low-temperature cryostat system. All refinements were performed via FULLPROF [53] using a Le Bail fit on the (00 l) face and assuming a monoclinic angle β of 90° . Thus, the spacing measured represents the layer spacing and is equal to the sum of one lamella and one van der Waals gap [54–57].

We employed a Quantum Design MPMS-7 superconducting quantum interference device magnetometer to take magnetization measurements. We found that the ambient-temperature dc resistivity to be in the megaohm range and that it increased with decreasing temperature, so was beyond the capability of our Quantum Design Physical Property Measurement System (PPMS). Based on these observations, and the optical study discussed below, we conclude the crystals are insulating. Heat-capacity measurements were made on as-grown single crystals using a Quantum Design PPMS at zero applied field for temperatures between 2.5 and 300 K.

The energy-dependent reflectivity was measured at discrete temperatures from room temperature to below the Néel temperature, $T_N \sim 120$ K. A Bruker Vertex 80v interferometer was employed across the wide spectral range from 70 cm^{-1} (~ 9 meV) to 25000 cm^{-1} (~ 3 eV) using several sources, beam splitters, and detectors [58]. The crystal was held in an exchange gas with the temperature controlled via a variable-temperature flow-through Oxford cryostat and when using liquid nitrogen as the coolant reaching 70 K. One unsubstituted sample was cooled to 15 K using liquid helium and no significant difference in behavior was observed below 70 K. The actual temperature of the sample was estimated to be no more than a few degrees above the measured temperature due mainly to the warming effect of the optical probe. The spectral resolution in the far-IR was 4 cm^{-1} rising to 16 cm^{-1} in the visible. The reflectivity was measured relative to an evaporated Al film and corrected using literature values for the aluminium reflectivity [59]. In all cases we measured the reflectivity of stacks of $\text{Co}_2\text{P}_2\text{S}_6$ crystals, grown with an ab plane alignment, and with the electric vector parallel to the 2D ab planes. The transmission of $\text{Co}_2\text{P}_2\text{S}_6$ was measured at 300 K to be zero except in one sample where we deliberately exfoliated a sample to transmit visible light. Although this sample was not a single crystal, and exhibited a range of thicknesses, the transmission measurement did help confirm the presence of absorption bands determined by analysis of the reflectivity spectra, particularly at high energy.

To account for the impact of the nonspecular reflecting surface on the photometric accuracy of the reflectivity measurement, the crystals, after the first measurement, were overcoated with Al and remeasured relative to the same Al reference resulting in a “corrected” reflectivity. Holmes and co-workers [60] have shown that this approach accounts reasonably well for the loss of light through scattering, and thus keeps systematic errors in the magnitude of the reflectivity to a minimum. As will be discussed below we find that correcting the reflectivity in this way does not fully account for the magnitude of the calculated conductivity; the temperature

dependence of the modes, such as the mode width and position, is very reliable.

The energy-dependent optical conductivity was generated by modeling the corrected reflectivity employing REFFIT software [61,62] and using a Kramers-Kronig consistent sum of Lorentzian functions to simulate an energy-dependent dielectric function, $\varepsilon(\omega) = \varepsilon_1(\omega) + i\varepsilon_2(\omega)$, where

$$\varepsilon(\omega) = \varepsilon_{\infty} + \sum_k \frac{S_k^2}{\omega_{0k}^2 - \omega^2 - i\gamma_k\omega}.$$

Here, ε_{∞} is the high-frequency dielectric constant, ω is the frequency, ω_0 is the oscillator frequency, S is the oscillator strength, k denotes the oscillator in question, and γ is the damping. Below, we discuss our results in terms of the energy-dependent conductivity, which is related to the dielectric function by $\sigma(\omega) = -i\omega\varepsilon(\omega)/4\pi$, which contains information about the response from the phonons, and the electronic transitions to incident light. As noted above, the transmission was measured on one thinned crystal, confirming the presence of some broad optical features we observed in the reflectivity at higher energies. Due to the inability to get substantial areas with the same thickness, this did not prove to be anything other than a qualitative support in identifying spectral features. Below, we focus on two spectral regions, at low energies (far-IR) where the response is dominated by the vibrational modes, and the near-IR–visible dominated by low-energy electronic transitions.

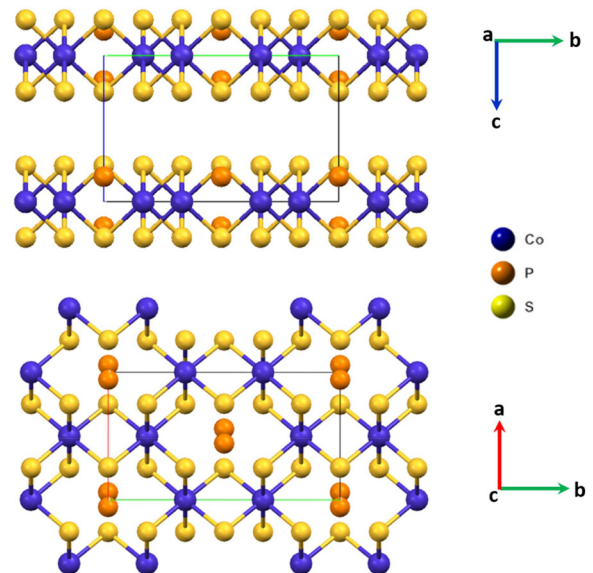


FIG. 1. The crystal structure of $\text{Co}_2\text{P}_2\text{S}_6$ viewed along the a axis (top), illustrating the 2D layers separated by a van der Waals gap, and along the c axis (bottom) illustrating the Co honeycomb lattice. Each Co atom is surrounded by six S atoms with the P dimers filling every third Co position and thereby sitting at the center of a Co honeycomb lattice. Note that each P atom of the dimer is connected to only three S atoms, thus with the dimer forming a P_2S_6 unit. The rectangles indicate a unit cell. The structure is based on published atomic positions [49] and was generated using the MERCURY software package from the Cambridge Crystallographic Data Centre (CCDC).

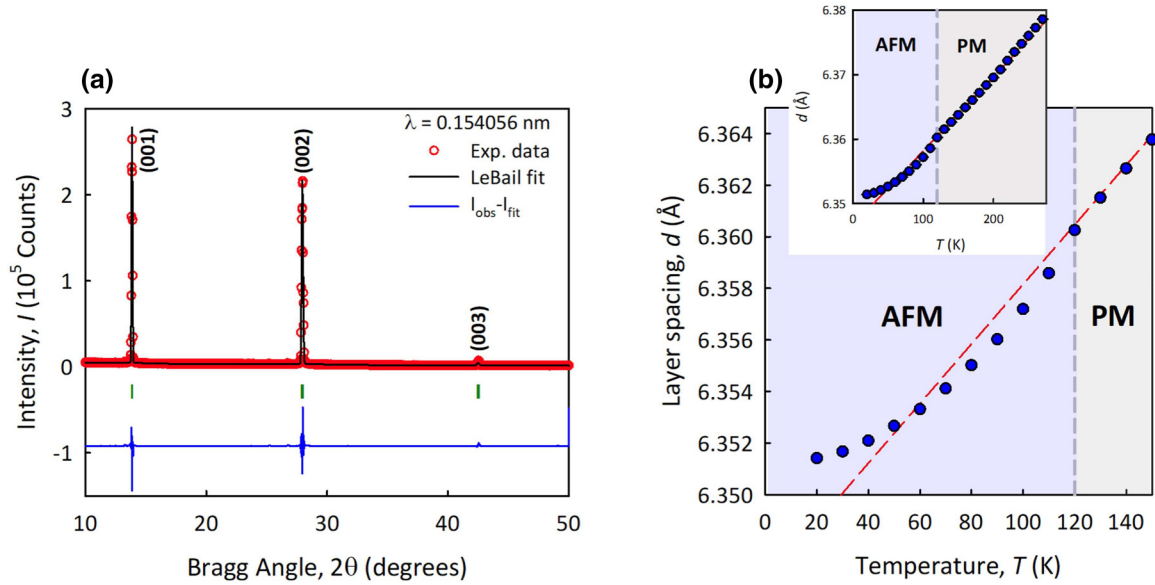


FIG. 2. (a) Out-of-plane θ - 2θ x-ray diffractograms for a crystal of $\text{Co}_2\text{P}_2\text{S}_6$ at 300 K. (b) Temperature dependence of the c -axis lattice parameter $\text{Co}_2\text{P}_2\text{S}_6$. XRD data collected with Cu $K\alpha$ radiation ($\lambda_{K\alpha 1} = 0.154056$ nm).

III. RESULTS

A. Structure

As shown in Fig. 1, the transition-metal chalcogenophosphate, $\text{Co}_2\text{P}_2\text{S}_6$, has a monoclinic structure with space group $C2/m$ [14,49]. These compounds consist of Co atoms surrounded by three (P_2S_6) units, such that the Co^{2+} ion and P-dimer are octahedrally coordinated to six chalcogen atoms. This results in the Co^{2+} ion occupying a 2D hexagonal honeycomb array surrounded by layers of S. These 2D layers, which are separated by the van der Waals gap, are stacked in an AAA sequence. The monoclinic angle is 107.17° , which is very close to the undistorted cell value [14].

As illustrated in Fig. 2(a), XRD patterns confirmed the presence of the $\text{Co}_2\text{P}_2\text{S}_6$ phase with an interlayer spacing of 0.638 346(25) nm at 300 K, which compares well with XRD and Transmission Electron Microscopy (TEM) experimental values of 0.6327 and 0.6545 nm, respectively, and a density-functional theory (DFT) value of 0.6402 nm [47]. Figure 2(b) displays the temperature dependence of the layer spacing measured down to ~ 20 K exhibiting a weak inflection at ~ 120 K (T_N). At T_N in FePS_3 the a axis contracts and b axis expands with an inflection in the layer spacing (i.e., $c \sin \beta$) as observed in Fig. 2(b) [63].

B. Magnetization and heat capacity

Figure 3(a) illustrates the magnetic susceptibility of unsubstituted and 40% Zn-substituted $\text{Co}_2\text{P}_2\text{S}_6$ crystals. The unsubstituted crystal exhibits an antiferromagnetic transition at ~ 120 K as has been previously reported [49], while we observe that when 40% of the Co is substituted by Zn there is a complete suppression of the long-range antiferromagnetic transition. As illustrated in Fig. 3(a), the Zn-substituted crystal exhibits paramagnetic behavior to the lowest temperatures measured (10 K). Chandrasekharan *et al.* [64] have shown that long-range correlated antiferromagnetism in $\text{Mn}_x\text{Zn}_{1-x}\text{PS}_3$ is

suppressed for Zn contents above the percolation threshold for a randomly diluted antiferromagnetic honeycomb lattice of $x = 0.7$, where the magnetic susceptibility can be accounted for by the uncompensated spins of the finite Mn^{2+} clusters. Our composition ($x = 0.6$) has slightly more Zn than the percolation threshold, ensuring that the long-range correlation is suppressed, while noting that these authors see evidence for the existence of short-range correlations for higher Zn contents than the percolation threshold [64].

As displayed in Fig. 3(b) there is a noticeable jump in the heat capacity in $\text{Co}_2\text{P}_2\text{S}_6$ single crystals consistent with the antiferromagnetic transition at ~ 120 K. Both the shape and magnitude of this anomaly are consistent with an antiferromagnetic transition. The magnitude of the transition is $\sim 31 \text{ J mol}^{-1} \text{ K}^{-1}$. This value is somewhat smaller than what is noted for $\text{Fe}_2\text{P}_2\text{S}_6$ ($\sim 65 \text{ J mol}^{-1} \text{ K}^{-1}$ [64]), which experiences a large structural transition concomitant with the onset of antiferromagnetism but, at the same time, larger than values seen in $\text{Mn}_2\text{P}_2\text{S}_6$ and $\text{Mn}_2\text{P}_2\text{Se}_6$ ($< 1 \text{ J mol}^{-1} \text{ K}^{-1}$ [65,66]) which experience no structural distortions associated with their antiferromagnetic transitions. These observations confirm (1) the presence of a small structural distortion as seen in the XRD analysis above, and (2) that it is smaller in magnitude than that seen for $\text{Fe}_2\text{P}_2\text{S}_6$. We plan on performing more detailed analyses on both the nature of this transition and its energetics using both XRD and specific-heat studies of the series of $(\text{Co}_{1-x}\text{Zn}_x)_2\text{P}_2\text{S}_6$ compounds in a future publication.

C. Phonon spectral region

Figure 4(a) illustrates the 230 K corrected reflectivity (black dots) over the spectral range 100 to 800 cm^{-1} (~ 0.01 to 0.1 eV) for $\text{Co}_2\text{P}_2\text{S}_6$ dominated by the IR-active vibrational modes involving atomic motion parallel to the ab plane. The temperature of 230 K was selected as it is well above the antiferromagnetic transition temperature. Also illustrated is the calculated reflectivity (red line) based on a dielec-

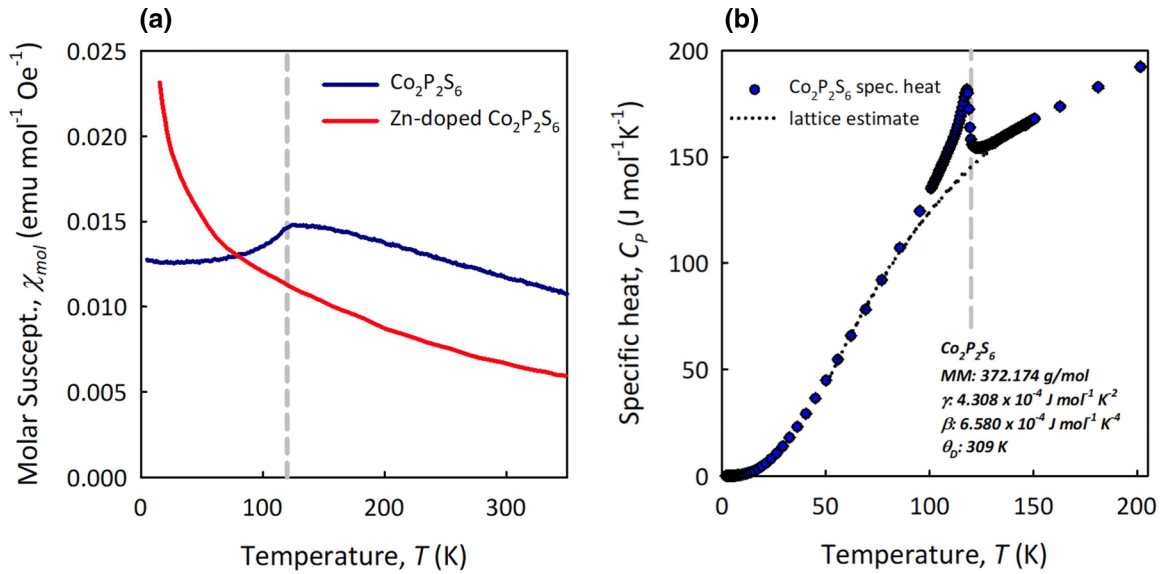


FIG. 3. (a) The temperature-dependent magnetic susceptibility of $\text{Co}_2\text{P}_2\text{S}_6$ (blue) and 40% Zn substituted for Co (red), when the field is orientated perpendicular to the ab plane. T_N for $\text{Co}_2\text{P}_2\text{S}_6$ is indicated at 120 K by the vertical gray dashed line illustrating the lack of a transition in the 40% Zn-substituted crystal. The small anomaly near 45 K is due to oxygen contamination. (b) The temperature dependence of the heat capacity for $\text{Co}_2\text{P}_2\text{S}_6$. The dotted line is an estimate of the lattice contribution highlighting the antiferromagnetic contribution at the transition temperature of ~ 120 K as indicated by the vertical gray dashed line.

tric model developed using REFFIT to be discussed below. Figure 4(b) illustrates the 70 K corrected reflectivity spectra (black) and its accompanying model (red). It has been shown that for $\text{Co}_2\text{P}_2\text{S}_6$ and for $\text{Zn}_2\text{P}_2\text{S}_6$ the zone-centered phonon modes have the representation $\Gamma = 8A_g + 7B_g + 6A_u + 9B_u$, thus exhibiting a total of 12 IR-active modes, and notably 5 A_u modes, after subtracting the three acoustic modes ($A_u + 2B_u$) [21–24,28].

As described above, the energy-dependent conductivity is determined by modeling the reflectivity data shown in Fig. 4. In the 300 to 400-cm⁻¹ spectral region, compared to the phonons, several broad and weak features can be observed in the reflectivity. We found that these features varied from

sample to sample and were stable with temperature [e.g., compare this spectral region in Fig. 4 and Fig. 6(a)]. We argue that the fringes are the result of optical interference in the micaceous crystal stacks. The fringes represent layers ranging in thickness from ~ 50 to 100 μm , which would be reasonable.

Figure 5(a) compares changes in the real part of the energy-dependent conductivity, $\sigma_1(\omega)$, for $\text{Co}_2\text{P}_2\text{S}_6$ at 230 K (red) and 70 K (blue) in crossing the antiferromagnetic transition, T_N at ~ 120 K. At temperatures between 230 K and to just above T_N all the vibrational modes are modeled with five Lorentzian oscillators and a high-energy dielectric constant that systematically decreases with temperature from 8.4 to 7.0 between 230 and 70 K. These latter values compare

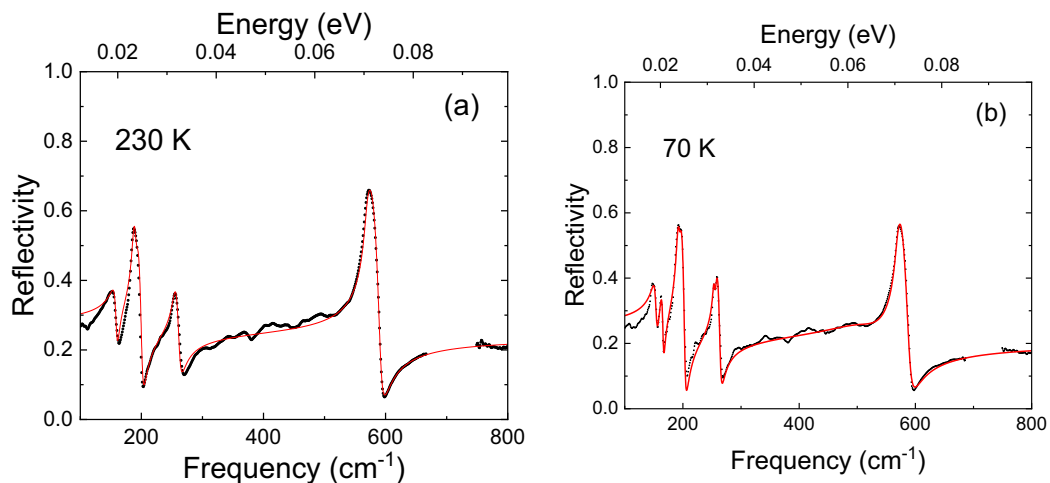


FIG. 4. The reflectivity of $\text{Co}_2\text{P}_2\text{S}_6$ crystals (black dots) for a temperature (a) above T_N at 230 K, and (b) a temperature below T_N at 70 K. The best-fit calculated reflectivity, based on the dielectric function described in the text, is also illustrated (red line).

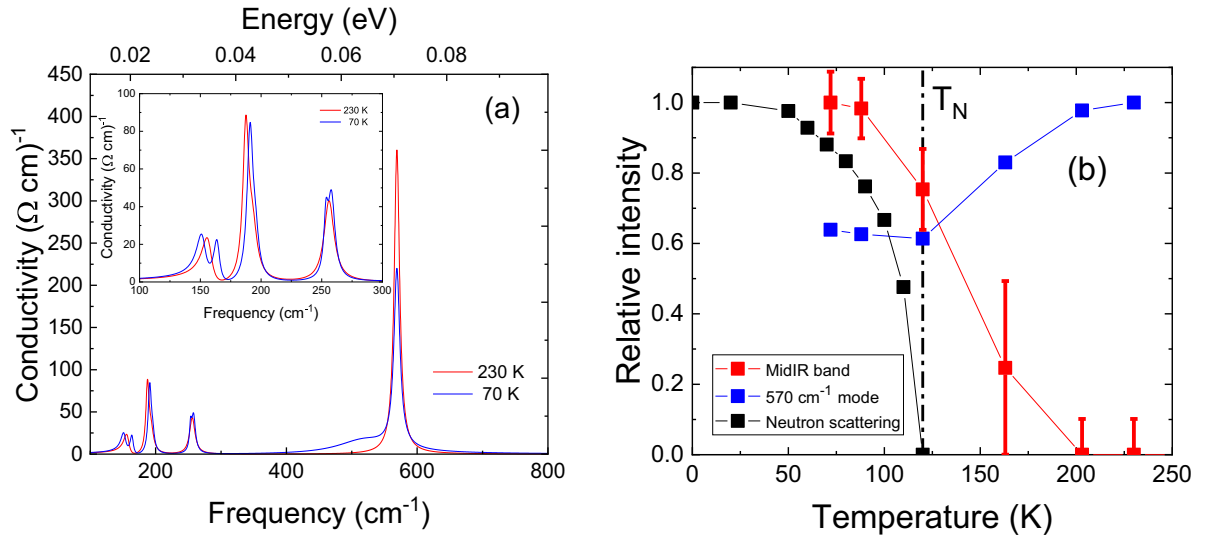


FIG. 5. (a) Comparing the energy-dependent conductivity, $\sigma_1(\omega)$, for $\text{Co}_2\text{P}_2\text{S}_6$ at 230 K (red) and 70 K (blue). There is an approximate 40% loss in oscillator strength in the 569-cm^{-1} mode. The inset highlights the low-energy region to emphasize the splitting and energy shifts of the low-energy modes below the transition temperature, T_N . (b) The temperature dependence of the relative spectral weight of the 569-cm^{-1} (blue) and the broad mid-IR band (red). The uncertainty in the spectral weight of the 569-cm^{-1} mode is $\sim 20\%$. We have also included the relative temperature dependence of the $(0,1,0)$ neutron-scattering Bragg peak (black) where the authors note that the error bars are smaller than the symbols [49].

well with values of ~ 9 for NiPS_3 [67] and are driven by higher-energy transitions including the low energy of the electronic transitions involving the d -level states to be discussed below. [See the temperature dependence of the modes summarized in Fig. 7(a) and the major atomic motions are listed in Table I.] The 569-cm^{-1} mode maintains its spectral position and width, but with decreasing temperature there is a loss in spectral weight that largely shifts to lower energies. Below T_N all the modes except the high-energy mode at 569 cm^{-1} resolve into two modes, reflecting the coupling between the magnetism and the lattice degrees of freedom. There is a weak narrowing of all the modes with decreasing temperature but it is always less than our spectral resolution. This applies even to the split modes that exhibit similar widths to their parent mode above T_N . The inset in Fig. 5(a) highlights the shifts and splitting of the low-energy modes in crossing T_N . We also observe that the 230 K low-energy mode at 157 cm^{-1} , which is dominated by the Co motion, is best modeled with a Fano line shape with an asymmetry parameter of 0.32 [68]. Below T_N this mode is replaced by two modes at 152 and 164 cm^{-1} , with asymmetry parameters of 0.28 and 0.16, respectively.

This indicates that these Co-dominated asymmetric vibrations are interacting with a broad electronic continuum that we will discuss further below. Although the “best” model below $\sim 200\text{ cm}^{-1}$ required a Fano line shape, we note the relatively poor “fit” below $\sim 140\text{ cm}^{-1}$ in Fig. 4. The match between the model and data could be improved by employing a Fano line shape and an energy-dependent loss that decreased with increasing energy, suggesting that surface features exist that enhance the loss at low energies.

Interestingly, from just above T_N and at lower temperatures, a broad absorption band had to be added to the model to fully describe the background spectral weight. As can be readily seen in the 70 K conductivity spectra (blue), there is a significant additional absorption in the ~ 400 to $\sim 650\text{-cm}^{-1}$ spectral range. The full width at half maximum (FWHM) is $\sim 100\text{ cm}^{-1}$, which is considerably broader in comparison to the vibrational modes, which in all cases exhibit a FWHM of less than 13 cm^{-1} . The temperature dependence of this absorption band is summarized in Fig. 5(b). Even with the correction to account for the nonspecular reflecting surface there are limits in determining the accuracy of the reflectiv-

TABLE I. A listing of the phonon-mode frequencies at 300 and 70 K for unsubstituted and Zn-substituted $\text{Co}_2\text{P}_2\text{S}_6$. The atomic motions are assigned as per the literature [21–24].

Atomic motion	Zn = 0		Zn = 40%	
	230 K mode frequency (cm^{-1})	70 K mode frequency (cm^{-1})	300 K mode frequency (cm^{-1})	70 K mode frequency (cm^{-1})
Co-S bending	157	152 and 164	135	135
P and S bending	187.5 and 193	191 and 195.5	184	184
Co-S stretching	256	253.5 and 258	258	258
P-P and S-P stretching	569	569	570	575 and 585

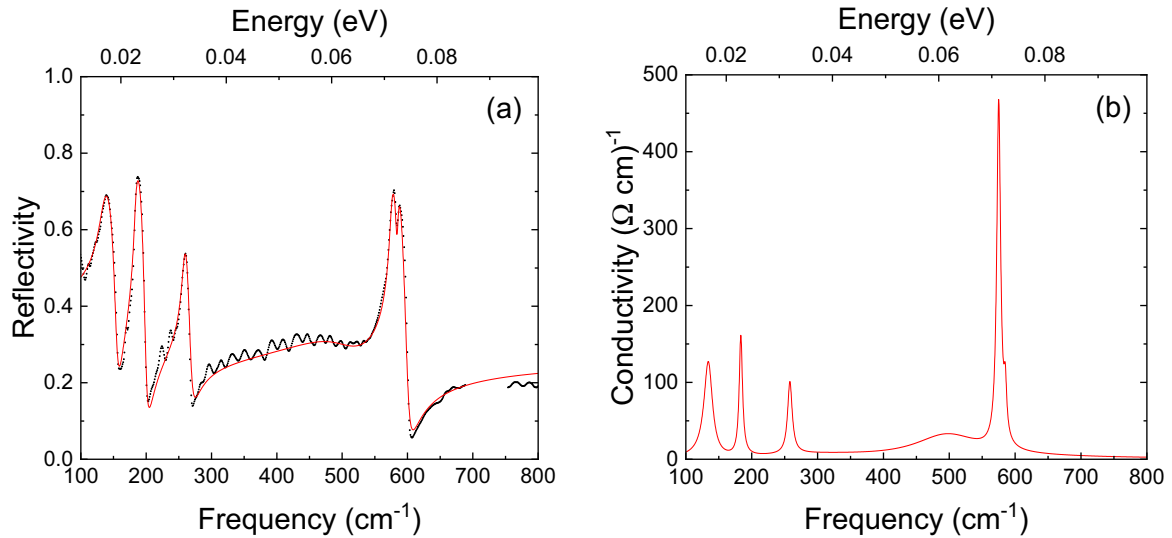


FIG. 6. (a) The 70 K reflectivity of 40% Zn substituted for Co in $\text{Co}_2\text{P}_2\text{S}_6$ (black) along with a model (red) discussed in the text. The weak oscillation in R between about 300 and 500 cm^{-1} we assign to interference fringes in the top layers of the exfoliated crystals. (b) The 70 K energy-dependent conductivity, $\sigma_1(\omega)$, of 40% Zn-substituted $\text{Co}_2\text{P}_2\text{S}_6$.

ity magnitude. The result is that a relatively large range of magnitudes for the broad mid-IR band gives a reasonable description of the data unlike the narrow phonon modes that are tightly defined. The vertical error bars in Fig. 5(b) quantify the uncertainty in the magnitude of the broad mid-IR band. They are particularly large just above the antiferromagnetic transition, ranging from zero to the top bar as required to adequately describe the data. While we estimate that the systematic error in the magnitude of the conductivity is approximately 20%, there is a noticeable net shift in oscillator strength from the 569- cm^{-1} mode to the mid-IR band for unsubstituted crystals. As is apparent in Fig. 5(a) this shift in oscillator strength only applies to the 569- cm^{-1} mode.

Figure 6(a) displays the 70 K reflectivity and corresponding model for a 40% Zn-substituted sample. Figure 6(b) displays the 70 K real part of the energy-dependent conductivity, $\sigma_1(\omega)$, for the same 40% Zn-substituted sample.

As demonstrated in Fig. 3, the long-range antiferromagnetic correlation in $\text{Co}_2\text{P}_2\text{S}_6$ is suppressed when 40% of the Co atoms are replaced by Zn and the temperature dependence observed in unsubstituted crystals effectively disappears. We observe significant changes in the vibrational modes, with 40% Zn substitution accompanying the suppression of long-range antiferromagnetic behavior. This is clearly illustrated by comparing the conductivity spectra in Figs. 5(a) and 6(b), the temperature dependency of the mode energies in Figs. 7(a) and 7(b), and as illustrated in Table I. The 569- cm^{-1} stretching mode now clearly resolves into two modes at 575 and 585 cm^{-1} . The high-energy stretching modes harden weakly with the two modes at 253.5 and 258 cm^{-1} replaced by a single mode at 258 cm^{-1} . A softening of about $\sim 10 \text{ cm}^{-1}$ on Zn substitution is observed for the bond-bending modes near 190 cm^{-1} which can now be modeled with a single oscillator. Notably, the low-energy bending Co-S mode at

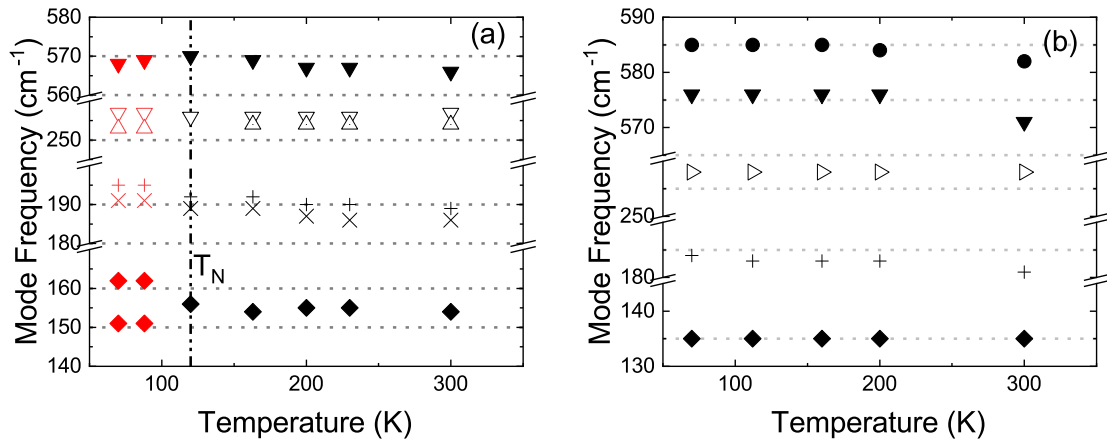


FIG. 7. (a) The temperature dependence of the vibrational modes in unsubstituted $\text{Co}_2\text{P}_2\text{S}_6$. The Néel temperature is indicated by the vertical dotted-dashed line at 120 K and the red points emphasize the impact of the magnetic transition on the phonons. (b) The temperature dependence of the phonons in 40% Zn-substituted $\text{Co}_2\text{P}_2\text{S}_6$ illustrating the lack of any change at the magnetic transition.

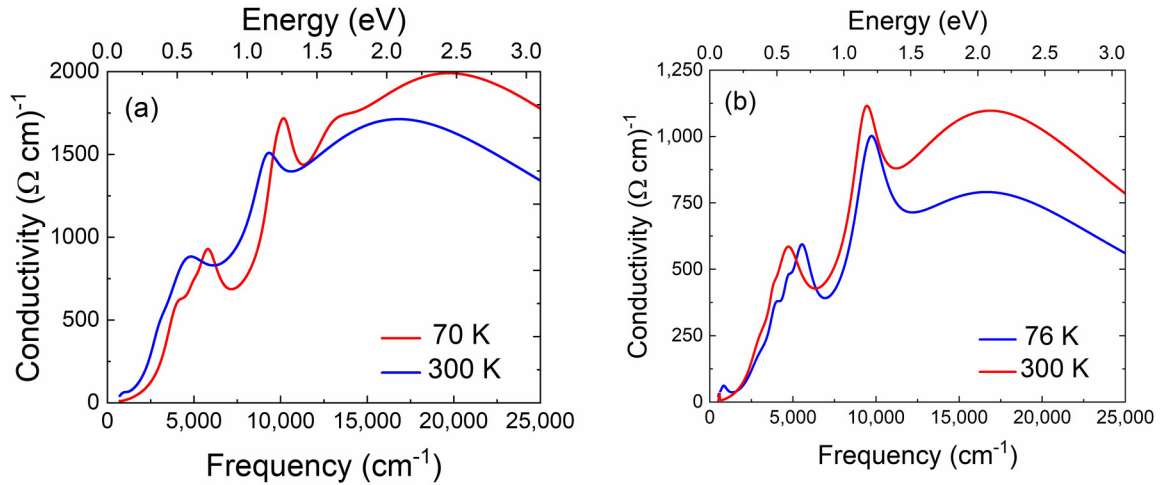


FIG. 8. (a) The high-energy energy-dependent conductivity at 300 K (red) and 72 K (blue) for $\text{Co}_2\text{P}_2\text{S}_6$ illustrating the change in its electronic behavior in passing through T_N . (b) The energy-dependent conductivity for $\text{Co}_2\text{P}_2\text{S}_6$ with 40% Co substitute by Zn at 300 and 76 K.

155 cm^{-1} in unsubstituted $\text{Co}_2\text{P}_2\text{S}_6$ does not resolve into two modes below 70 K and is $\sim 20 \text{ cm}^{-1}$ softer on Zn substitution. Moreover, its asymmetry is significantly reduced, compared to unsubstituted crystals, being 0.06. The damping of all the modes is relatively unchanged with Zn substitution, the exception being the low-energy Co-bending mode, which exhibits a much larger damping, ranging from ~ 15.5 to 21 cm^{-1} over the 70 to 300 K temperature range. For unsubstituted $\text{Co}_2\text{P}_2\text{S}_6$, and above T_N , the damping of this mode is no more than 10 cm^{-1} and below T_N splits into two modes with damping of 6 and 10 cm^{-1} . To fit the spectra, and as indicated in Fig. 6(b), a broad mid-IR mode is also required at the lowest temperatures of 112 and 72 K in 40% Zn-substituted $\text{Co}_2\text{P}_2\text{S}_6$. In unsubstituted $\text{Co}_2\text{P}_2\text{S}_6$ we assigned this feature to localized magnon fluctuations as observed in neutron scattering reported in $\text{Co}_2\text{P}_2\text{S}_6$ [50] and in magnetization studies [64]. The analysis of the optical data in Fig. 6(b) would suggest that localized magnon fluctuations also exist in Zn substitute crystals, although the long-range antiferromagnetic correlations are suppressed.

D. Electronic transitions

Figure 8(a) displays at high energy ($> 0.1 \text{ eV}$) the energy-dependent conductivity for $\text{Co}_2\text{P}_2\text{S}_6$ at 300 K (red) and 72 K (blue). As discussed above, this parameter was derived from a corrected reflectivity measurement, which was modeled using a dielectric function, $\epsilon(\omega)$, employing a series of oscillators in REFFIT. We note that some of the temperature-dependent differences in the magnitude of the optical conductivity will be due to the light beam moving on the sample with changing temperature so that the resulting variations in light scattering were not fully accounted for. Nonetheless, repeated measurements, and in some cases on different crystals, show that the absorption-band frequencies are reproducible. Figure 8(a) shows that the low-energy absorption in $\text{Co}_2\text{P}_2\text{S}_6$ is very low and consistent with the measured very high dc resistivity, confirming that $\text{Co}_2\text{P}_2\text{S}_6$ is an insulator. The absorption extrapolates to zero at $0.20 \pm 0.02 \text{ eV}$ at 300 K and blueshifts at 70 K to $0.31 \pm 0.02 \text{ eV}$. As illustrated in Fig. 8(b) for the

Zn substitute crystals, the absorption extrapolates to zero at $0.19 \pm 0.02 \text{ eV}$ at 300 K and to $0.18 \pm 0.02 \text{ eV}$ at 76 K, indicating that within experimental error these are the same absorption onset energies as observed at 300 K in the unsubstituted $\text{Co}_2\text{P}_2\text{S}_6$.

As listed in Table II, and illustrated in Fig. 8(a), four oscillators are required to model the 300 K $\text{Co}_2\text{P}_2\text{S}_6$ reflectivity. The center energies of the absorption bands were in part confirmed by the 300 K transmission measurements, where we see transmission minima centered at 0.39, 0.55, and 0.90 eV along with a large absorption onset that extrapolates to zero near 1.6 eV. The two lowest-energy bands fall at the same position as determined by both the transmission and reflectivity spectra, while we assign the 0.9-eV transmission minima to be the same feature as the 1.14-eV band in the conductivity spectra. An effective shift to a higher energy will be driven by use of model Lorentzians, with their large tails, in modeling

TABLE II. Tabulation of the oscillator energies (eV) derived from modeling the reflectivity spectra of $\text{Co}_2\text{P}_2\text{S}_6$ and 40% Zn-substituted $\text{Co}_2\text{P}_2\text{S}_6$ at temperatures above and below the antiferromagnetic transition temperature. Transmission measurements confirm the presence of bands for 300 K $\text{Co}_2\text{P}_2\text{S}_6$ at 0.55 and 0.39 eV and indicate that the 1.14-eV band in fact lies at 0.9 eV as discussed in the text. The width of the bands at 2.48 and 2.12 eV are at least ten times the width ($\sim 3 \text{ eV}$) of all the low-energy bands ($< 0.3 \text{ eV}$), suggesting a different physical process. Clearly the presence of an antiferromagnetic transition determines the number of electronic absorption bands observed.

Electronic absorption energies (eV)			
0% Zn		40% Zn	
72 K	300K	76 K	300K
2.48	2.12	2.12	2.12
1.61	1.14	1.20	1.16
1.23	0.55	0.67	0.59
0.72	0.39	0.49	0.38
0.61			
0.50			

the reflectivity when there is a nearby strong absorption band. Identifying band energies can be determined directly from the local minimum in transmission spectra. Thus, the strong band centered at 2.12 eV, where our model requires a large tail to low energy, results in an effective shift from 0.9 eV (transmission) to 1.14 eV (reflectivity). In Table II we have kept the band positions determined by modeling the reflectivity so we can compare spectra on different samples and temperatures where we do not have transmission measurements. In previous reports the band at 0.9 eV has been reported but the two low-energy bands have not been reported [37–40]. At 72 K there is an observable increase to six oscillators required to fit the reflectivity. Figure 8(b) displays the energy-dependent conductivity for 40% Zn-substituted $\text{Co}_2\text{P}_2\text{S}_6$ at 300 K (red) and 76 K (blue). With 40% Zn substitution and at 300 K the reflectivity can be modeled with four oscillators. At 76 K it is notable that only four oscillators are required to model the reflectivity. The temperature dependence with Zn substitution is not large although there is a small hardening of the three low-energy oscillators and a 16% loss of strength for the high-energy band. Interestingly, the same number of oscillators model the 300 K reflectivity for 0% Zn substitution, and the 300 and 76 K reflectivity for 40% Zn substitution. Within experimental error the position of the bands is very nearly the same when the long-range antiferromagnetic correlation is not present (see Table II). We also note that the widths (~ 3 eV) of the highest-energy bands, at 2.48 and 2.12 eV, in the 72 and 300 K data respectively, are ten times the widths (< 0.3 eV) of all the low-energy bands, suggesting different physical processes.

IV. DISCUSSION

There have been several reflection and transmission-absorption studies of the high-energy optical response (> 0.1 eV) of $\text{Co}_2\text{P}_2\text{S}_6$, although carried out over limited energy ranges and thus lacking complete agreement about the number, positions, and the assignments of the electronic absorption bands [37–40]. Based on transmission and reflectivity measurements, and the derived optical conductivity, we have determined, over a wide energy range (0.1 to 3 eV), the low-energy electronic absorption band energies (listed in Table II), and their widths. DFT band-structure calculations on $\text{Co}_2\text{P}_2\text{S}_6$, including onsite Coulomb interactions, show that the upper valence band is formed from hybrid S and Co states, involving a $\sim 25\%$ Co $3d$ contribution. The lower conduction band is composed largely of Co $3d$ states with a smaller contribution from the S $3p$ states [47,48]. These band-structure calculations exhibit narrow $3d$ Co bands of low dispersion consistent, with the 2D structure and the magnetic measurements indicating strongly localized $3d$ moments. Thus, we assign the three narrow absorption bands observed in the 300 K spectra in both compositions, and the 76 K spectra for the Zn-substituted crystal, below about 1.5 eV, to transitions between localized $3d$ Co states. We note that the highest-energy, strongly absorbing bands, above ~ 2 eV, which exhibit much larger widths, are transitions between either valence or conduction s states and $3d$ Co states with an optical onset energy of ~ 1.6 eV as defined by our transmission spectra. The lowest-energy electronic absorption onset is however, 0.20 ± 0.02 eV arising from spectrally narrow transitions

between $3d$ levels. These results suggests that the band-structure calculations need to be revised.

The number and energy of the strongly localized $3d$ states depend on the lattice symmetry around the Co^{2+} ion and the magnitude of the superexchange energy (coupling via the six sulfur atoms) [46]. Thus, the onset of antiferromagnetic order will reduce the local symmetry, further splitting of the Co^{2+} $3d$ states, and leading to an increase in the number of absorption bands as we observed in Fig. 8(a). The lowering in energy of the occupied states at T_N will also accommodate a lattice or Jahn-Teller distortion around the Co^{2+} ion as is observed, for instance, in FePS_3 [63]. The 300 K optical spectra of unsubstituted and 40% Zn-substituted $\text{Co}_2\text{P}_2\text{S}_6$ at 300 and 76 K are very similar with three absorption bands at the same energies, while spectra for the unsubstituted sample below T_N exhibit five absorption bands, clearly demonstrating the correlation between the electronic and magnetic degrees of freedom.

We also observe significant coupling between the IR-active lattice vibrations and the magnetism of $\text{Co}_2\text{P}_2\text{S}_6$. First, a very clear observation is the sudden increase in the number of vibrational modes, from 5 to 7, at the antiferromagnetic transition. The low-energy modes that split at T_N involve significant Co motion at 257 cm^{-1} (Co-S stretching) and at 154 cm^{-1} (Co-S bending). Little or no temperature dependence is observed for the position of the high-energy mode at 569 cm^{-1} , which is dominated by P-P and S-P stretching motion. Moreover, no temperature-dependent changes in any of the modes in 40% Zn-substituted $\text{Co}_2\text{P}_2\text{S}_6$ are observed down to ~ 70 K, where the long-range antiferromagnetism, as illustrated in Fig. 3, is suppressed. The increase in the number of modes at T_N in unsubstituted $\text{Co}_2\text{P}_2\text{S}_6$ is consistent with a commensurate transition to a lower-symmetry structure associated primarily with the onset of a long-range antiferromagnetic correlation. A signature of such an induced structural transition is observed in the small inflection in the c -axis data in Fig. 2(b). Second, the low-energy IR-active vibrations, exhibiting large Co motion, are asymmetric, unlike the high-energy modes, indicating coupling between a narrow phonon mode, involving Co motion, and an electronic continuum [68]. Third, the 20-cm^{-1} softening of the low-energy modes accompanies the suppression of the antiferromagnetic transition on 40% Zn substitution. Fourth, we observe that the high-energy mode at 569 cm^{-1} also loses significant spectral weight with decreasing temperature down to T_N . This mode involves S-P stretching motion where S is involved in the superexchange between neighboring Co^{2+} ions. Fifth, the presence of a broad IR absorption band ranging from $\sim 400\text{ cm}^{-1}$ (50 meV) to $\sim 650\text{ cm}^{-1}$ (80 meV) that rapidly increases in strength from just above T_N . IR coupling between phonons and magnons has been reported in antiferromagnets such as NiO via a multiphonon-assisted 2-magnon IR absorption process [69–71]. For instance, assuming coupling between the single low-energy Co-bending mode at 155 cm^{-1} (19 meV), and the magnon spectrum ranging in energy from 15 to 35 meV [50], then the expected phonon-assisted 2-magnon IR absorption band would run from 50 to 90 meV, i.e., ~ 400 to $\sim 720\text{ cm}^{-1}$, which is close to the observed mid-IR band we report in Fig. 5(a). Raman scattering from magnons in $\text{Co}_2\text{P}_2\text{S}_6$ has also been reported [12,30,50].

V. CONCLUSIONS

We report the temperature-dependent IR-active, *ab*-plane, vibrational modes and the low-energy electronic transitions while crossing the antiferromagnetic transition at ~ 120 K in unsubstituted and 40% Zn-substituted $\text{Co}_2\text{P}_2\text{S}_6$. The low-energy modes exhibit significant sensitivity to the antiferromagnetic transition. The lowest-energy mode at 157 cm^{-1} , dominated by Co motion, resolves into two modes at T_N , and exhibits an asymmetric line shape, indicating coupling to an underlying electronic continuum. With 40% Zn substitution for Co this low-energy 157-cm^{-1} mode softens by 20 cm^{-1} , while none of the phonons exhibit any anomalies with temperature down to 70 K, consistent with the suppression of the long-range antiferromagnetic correlations. We also report at temperatures near and below T_N the presence of a broad ($\sim 250\text{ cm}^{-1}$) IR-active absorption band. The width of this band is many times the phonon linewidth of under 13 cm^{-1} . The energy range of this band is consistent with an interaction with magnons, which are reported in neutron-scattering experiments on $\text{Co}_2\text{P}_2\text{S}_6$. We have thus proposed that the optical spectroscopy is probing the magnons via a phonon plus 2-magnon absorption process as observed in other antiferromagnets such as NiO [69]. We also find that the symmetry of the $3d$ states in an octahedral crystal field is lowered further in the antiferromagnetic state, resulting in an increase in the number of electronic absorption bands observed in unsubstituted $\text{Co}_2\text{P}_2\text{S}_6$. This lowering in symmetry drives a yet-unobserved change in the *ab*-plane lattice parameters, perhaps like that observed in FePS_3 [63]. The temperature-dependent changes in the optical response indicate strongly correlated behavior between the

infrared-active lattice vibrations, the electronic excitations, and magnetism in unsubstituted $\text{Co}_2\text{P}_2\text{S}_6$.

ACKNOWLEDGMENTS

This research was supported by a University Research Fund grant from Victoria University of Wellington. The MacDiarmid Institute for Advanced Materials and Nanotechnology is supported under the New Zealand Centres of Research Excellence Programme. This research was additionally supported by the Air Force Office of Scientific Research (AFOSR), Grant No. LRIR23RCOR003, and AOARD-NSTC, Grant No. F4GGA21207H002. We also acknowledge support from the National Research Council's Senior NRC Associateship program sponsored by the National Academies of Science, Engineering, and Medicine and administered by the AFRL Sensors Directorate. Low-temperature x-ray-diffraction measurements (M.A.M.) were supported by the U.S. Department of Energy, Office of Science, Basic Energy Sciences, Materials Sciences and Engineering Division.

This manuscript has been coauthored by employees of UT-Battelle, LLC under Contract No. DE-AC05-00OR22725 with the U.S. Department of Energy. The United States Government retains, and the publisher, by accepting the article for publication, acknowledges, that the United States Government retains a nonexclusive, paid-up, irrevocable, worldwide license to publish or reproduce the published form of this manuscript, or allow others to do so, for United States Government purposes. The Department of Energy will provide public access to these results of federally sponsored research in accordance with the DOE Public Access Plan [72].

-
- [1] N. F. Mott, The basis of the electron theory of metals, with special reference to the transition metals, *Proc. Phys. Soc. Sect. A* **62**, 416 (1949).
- [2] J. Zaanen, G. A. Sawatzky, and J. W. Allen, Band gaps and electronic structure of transition-metal compounds, *Phys. Rev. Lett.* **55**, 418 (1985).
- [3] S. Y. Kim, T. Y. Kim, L. J. Sandilands, S. Sinn, M.-C. Lee, J. Son, S. Lee, K.-Y. Choi, W. Kim, B.-G. Park *et al.*, Charge-spin correlation in van der Waals antiferromagnet NiPS_3 , *Phys. Rev. Lett.* **120**, 136402 (2018).
- [4] Y. Wang, J. Ying, Z. Zhou, J. Sun, T. Wen, Y. Zhou, N. Li, Q. Zhang, F. Han, Y. Xiao *et al.*, Emergent superconductivity in an iron-based honeycomb lattice initiated by pressure-driven spin-crossover, *Nat. Commun.* **9**, 1914 (2018).
- [5] Y. Gu, Q. Zhang, C. Le, Y. Li, T. Xiang, and J. Hu, Ni-Based transition metal trichalcogenide monolayer: A strongly correlated quadruple-layer graphene, *Phys. Rev. B* **100**, 165405 (2019).
- [6] X. Jiang, Q. Liu, J. Xing, N. Liu, Y. Guo, Z. Liu, and J. Zhao, Recent progress on 2D magnets: Fundamental mechanism, structural design and modification, *Appl. Phys. Rev.* **8**, 031305 (2021).
- [7] N. Sheremetyeva, I. Na, A. Saraf, S. M. Griffin, and G. Hautier, Prediction of topological phases in metastable ferromagnetic MPX_3 monolayers, *Phys. Rev. B* **107**, 115104 (2023).
- [8] R. Brec, D. M. Schleich, G. Ouvrard, A. Louisy, and J. Rouxel, Physical properties of lithium intercalation compounds of the layered transition-metal chalcogenophosphites, *Inorg. Chem.* **18**, 1814 (1979).
- [9] F. M. Oliveira, J. Paštika, V. Mazánek, M. Melle-Franco, Z. Sofer, and R. Gusmão, Cobalt phosphorous trisulfide as a high-performance electrocatalyst for the oxygen evolution reaction, *ACS Appl. Mater. Interfaces* **13**, 23638 (2021).
- [10] R. Samal, G. Sanyal, B. Chakraborty, and C. S. Rout, Two-dimensional transition metal phosphorous trichalcogenides (MPX_3): A review on emerging trends, current state and future perspectives, *J. Mater. Chem. A* **9**, 2560 (2021).
- [11] K. F. Mak, J. Shan, and D. C. Ralph, Probing and controlling magnetic states in 2D layered magnetic materials, *Nat. Rev. Phys.* **1**, 646 (2019).
- [12] P. Liu and Y. Pu, Construction of two-dimensional CoPS_3 @defective N-doped carbon composites for enhanced oxygen evolution reaction, *Int. J. Hydrog. Energy* **47**, 197 (2022).
- [13] M. A. Susner, M. Chyashnavichyus, M. A. McGuire, P. Ganesh, and P. Maksymovych, Metal thio- and selenophosphates as multifunctional van der Waals layered materials, *Adv. Mater.* **29**, 1602852 (2017).
- [14] G. Ouvrard, R. Brec, and J. Rouxel, Structural determination of some MPS_3 layered phases ($M = \text{Mn, Fe, Co, Ni}$ and Cd), *Mater. Res. Bull.* **20**, 1181 (1985).

- [15] R. Brec, Review on structural and chemical properties of transition metal phosphorus trisulfides MPS_3 , *Solid State Ion.* **22**, 3 (1986).
- [16] J.-U. Lee, S. Lee, J. H. Ryoo, S. Kang, T. Y. Kim, P. Kim, C.-H. Park, J.-G. Park, and H. Cheong, Ising-type magnetic ordering in atomically thin FePS_3 , *Nano Lett.* **16**, 7433 (2016).
- [17] G. Long, H. Henck, M. Gibertini, D. Dumcenco, Z. Wang, T. Taniguchi, K. Watanabe, E. Giannini, and A. F. Morpurgo, Persistence of magnetism in atomically thin MnPS_3 crystals, *Nano Lett.* **20**, 2452 (2020).
- [18] N. Sivasdas, M. W. Daniels, R. H. Swendsen, S. Okamoto, and D. Xiao, Magnetic ground state of semiconducting transition-metal trichalcogenide monolayers, *Phys. Rev. B* **91**, 235425 (2015).
- [19] A. Scheie, P. Park, J. W. Villanova, G. E. Granroth, C. L. Sarkis, H. Zhang, M. B. Stone, J.-G. Park, S. Okamoto, T. Berlijn, and D. A. Tennant, Spin wave Hamiltonian and anomalous scattering in NiPS_3 , *Phys. Rev. B* **108**, 104402 (2023).
- [20] A. H. Thompson and M. S. Whittingham, Transition metal phosphorus trisulfides as battery cathodes, *Mater. Res. Bull.* **12**, 741 (1977).
- [21] Y. Mathey, R. Clement, C. Sourisseau, and G. Lucazeau, Vibrational study of layered MPX_3 compounds and of some intercalates with $\text{Co}(\eta^5\text{-C}_5\text{H}_5)^{2+}$ or $\text{Cr}(\eta^6\text{-C}_6\text{H}_6)^{2+}$, *Inorg. Chem.* **19**, 2773 (1980).
- [22] C. Sourisseau, J. P. Forgerit, and Y. Mathey, Vibrational study of the $[\text{P}_2\text{S}_6^{4-}]$ anion, of some MPS_3 layered compounds ($\text{M} = \text{Fe}, \text{Co}, \text{Ni}, \text{In}_{2/3}$), and of their intercalates with $[\text{Co}(\eta^5\text{-C}_5\text{H}_5)_2^+]$ cations, *J. Solid State Chem.* **49**, 134 (1983).
- [23] C. Sourisseau, J. P. Forgerit, and Y. Mathey, Vibrational study of layered ZnPS_3 compounds intercalated with $[\text{Co}(\eta^5\text{-C}_5\text{H}_5)_2^+]$ and $[\text{Cr}(\eta^6\text{-C}_6\text{H}_6)_2^+]$, *J. Phys. Chem. Solids* **44**, 119 (1983).
- [24] M. Bernasconi, G. L. Marra, G. Benedek, L. Miglio, M. Jouanne, C. Julien, M. Scagliotti, and M. Balkanski, Lattice dynamics of layered MPX_3 ($\text{M} = \text{Mn}, \text{Fe}, \text{Ni}, \text{Zn}$; $\text{X} = \text{S}, \text{Se}$) compounds, *Phys. Rev. B* **38**, 12089 (1988).
- [25] M. Jouanne and C. Julien, Fourier transform infrared spectroscopy studies at low temperatures of MPX_3 layered compounds, *J. Appl. Phys.* **64**, 3637 (1988).
- [26] P. A. Joy and S. Vasudevan, Infrared ($700\text{-}100\text{ cm}^{-1}$) vibrational spectra of the layered transition metal thiophosphates, MPS_3 ($\text{M} = \text{Mn}, \text{Fe}$ and Ni), *J. Phys. Chem. Solids* **54**, 343 (1993).
- [27] M. Scagliotti, M. Jouanne, M. Balkanski, G. Ouvrard, and G. Benedek, Raman scattering in antiferromagnetic FePS_3 and FePSe_3 crystals, *Phys. Rev. B* **35**, 7097 (1987).
- [28] R. Oliva, E. Ritov, F. Horani, I. Etxebarria, A. K. Budniak, Y. Amouyal, E. Lifshitz, and M. Guennou, Lattice dynamics and in-plane antiferromagnetism in $\text{Mn}_x\text{Zn}_{1-x}\text{PS}_3$ across the entire composition range, *Phys. Rev. B* **107**, 104415 (2023).
- [29] K. Kim, J.-U. Lee, and H. Cheong, Raman spectroscopy of two-dimensional magnetic van der Waals materials, *Nanotechnology* **30**, 452001 (2019).
- [30] Q. Liu, L. Wang, Y. Fu, X. Zhang, L. Huang, H. Su, J. Lin, X. Chen, D. Yu, X. Cui *et al.*, Magnetic order in XY-type antiferromagnetic monolayer CoPS_3 revealed by Raman spectroscopy, *Phys. Rev. B* **103**, 235411 (2021).
- [31] G. Benedek, G. L. Marra, L. Miglio, M. Scagliotti, and M. Jouanne, Lattice dynamics of layered crystals in the class MPX_3 ($\text{M} = \text{Fe}, \text{Mn}$; $\text{X} = \text{Se}, \text{S}$), *Phys. Scr.* **37**, 759 (1988).
- [32] A. Hashemi, H.-P. Komsa, M. Puska, and A. V. Krasheninnikov, Vibrational properties of metal phosphorus trichalcogenides from first-principles calculations, *J. Phys. Chem. C* **121**, 27207 (2017).
- [33] T. Babuka, M. Makowska-Janusik, A. V. Peschanskii, K. E. Glukhov, S. L. Gnatchenko, and Yu. M. Vysochanskii, Electronic and vibrational properties of pure MnPS_3 crystal: Theoretical and experimental investigation, *Comput. Mater. Sci.* **177**, 109592 (2020).
- [34] M. Piacentini, F. S. Khumalo, C. G. Olson, J. W. Andereg, and D. W. Lynch, Optical transitions, XPS, and electronic states in nickel phosphorus sulfide (NiPS_3), *Chem. Phys.* **65**, 289 (1982).
- [35] M. Piacentini, F. S. Khumalo, G. Leveque, C. G. Olson, and D. W. Lynch, X-ray photoemission and optical spectra of nickel phosphide sulfide (NiPS_3), iron phosphide sulfide (FePS_3) and zinc phosphide sulfide (ZnPS_3), *Chem. Phys.* **72**, 61 (1982).
- [36] F. S. Khumalo and H. P. Hughes, Reflectance spectra of some FePS_3 -type layer compounds in the vacuum ultraviolet, *Phys. Rev. B Condens. Matter Mater. Phys.* **23**, 5375 (1981).
- [37] V. Grasso, S. Santangelo, and M. Piacentini, Optical absorption spectra of some transition metal thiophosphates, *Solid State Ion.* **20**, 9 (1986).
- [38] E. Banda, Optical absorption of CoPS_3 in the energy range 0.73 to 5.40 eV, *Phys. Status Solidi B* **135**, K43 (1986).
- [39] D. A. Cleary and A. H. Francis, Analysis of the Mid-IR electronic absorption spectra of iron thiohypophosphate ($\text{Fe}_2\text{P}_2\text{S}_6$) and cobalt thiohypophosphate ($\text{Co}_2\text{P}_2\text{S}_6$), *J. Phys. Chem.* **92**, 2415 (1988).
- [40] N. Nagasundaram and A. H. Francis, FTIR electronic spectra of iron thiohypophosphate ($\text{Fe}_2\text{P}_2\text{S}_6$) and cobalt thiohypophosphate ($\text{Co}_2\text{P}_2\text{S}_6$): Trigonal field splitting and lithium intercalation effects, *J. Phys. Chem. Solids* **50**, 163 (1989).
- [41] V. Grasso, F. Neri, P. Perillo, L. Silipigni, and M. Piacentini, Optical-absorption spectra of crystal-field transitions in manganese thiophosphate (MnPS_3) at low temperatures, *Phys. Rev. B* **44**, 11060 (1991).
- [42] V. Grasso, F. Neri, L. Silipigni, and M. Piacentini, NIR-VIS reflectivity spectra of some transition metal thiophosphates, *Nuovo Cimento D* **13**, 633 (1991).
- [43] H. Mercier, Y. Mathey, and E. Canadell, On the electronic structure of MPS_3 phases, *Inorg. Chem.* **26**, 963 (1987).
- [44] N. Kurita and K. Nakao, Band structure of magnetic layered semiconductor nickel phosphide sulfide (NiPS_3), *J. Phys. Soc. Jpn.* **58**, 232 (1989).
- [45] N. Kurita and K. Nakao, Self-consistent band structure of layered semiconductor zinc thiohypophosphate (ZnPS_3), *J. Phys. Soc. Jpn.* **56**, 4455 (1987).
- [46] V. Zhukov, S. Alvarez, and D. Novikov, Electronic band structure of the magnetic layered semiconductors MPS_3 ($\text{M} = \text{Mn}, \text{Fe}$ and Ni), *J. Phys. Chem. Solids* **57**, 647 (1996).
- [47] Y. Jin, Y. Jin, K. Li, M. Yan, Y. Guo, Y. Zhou, A. Preobrajenski, Y. Dedkov, and E. Voloshina, Mixed insulating state for van der Waals CoPS_3 , *J. Phys. Chem. Lett.* **13**, 10486 (2022).
- [48] Y. Gu, S. Zhang, and X. Zou, Tunable magnetism in layered CoPS_3 by pressure and carrier doping, *Sci. Chi. Mater.* **64**, 673 (2021).
- [49] A. R. Wildes, V. Simonet, E. Ressouche, R. Ballou, and G. J. McIntyre, The magnetic properties and structure of the quasi-two-dimensional antiferromagnet CoPS_3 , *J. Phys.: Condens. Matter* **29**, 455801 (2017).

- [50] C. Kim, J. Jeong, P. Park, T. Masuda, S. Asai, S. Itoh, H.-S. Kim, A. Wildes, and J.-G. Park, Spin waves in the two-dimensional honeycomb lattice XXZ-type van der Waals antiferromagnet CoPS_3 , *Phys. Rev. B* **102**, 184429 (2020).
- [51] A. R. Wildes, M. J. Harris, and K. W. Godfrey, Two-dimensional critical fluctuations in MnPS_3 , *J. Magn. Magn. Mater.* **177** 143 (1998).
- [52] T. Matsuoka, R. Rao, M. A. Susner, B. S. Conner, D. Zhang, and D. Mandrus, Pressure-induced insulator-to-metal transition in the van der Waals compound CoPS_3 , *Phys. Rev. B* **107**, 165125 (2023).
- [53] C. Frontera and J. Rodriguez-Carvajal, FULLPROF as a new tool for flipping ratio analysis: Further improvements, *Phys. B* **350**, e731 (2004).
- [54] M. McGuire, Crystal and magnetic structures in layered, transition metal dihalides and trihalides, *Crystals* **7**, 121 (2017).
- [55] M. A. Susner, A. Belianinov, A. Borisevich, Q. He, M. Chyashvichyus, H. Demir, D. S. Sholl, P. Ganesh, D. L. Abernathy, M. A. McGuire *et al.*, High T_C layered ferroelectric crystals by coherent spinodal decomposition, *ACS Nano* **9**, 12365 (2015).
- [56] M. A. Susner, R. Rao, A. T. Pelton, M. V. McLeod, and B. Maruyama, Temperature-dependent Raman scattering and x-ray diffraction study of phase transitions in layered multiferroic CuCrP_2S_6 , *Phys. Rev. Mater.* **4**, 104003 (2020).
- [57] M. A. McGuire, H. Dixit, V. R. Cooper, and B. C. Sales, Coupling of crystal structure and magnetism in the layered, ferromagnetic insulator CrI_3 , *Chem. Mater.* **27**, 612 (2015).
- [58] R. G. Buckley, T. Butler, C. Pot, N. M. Strickland, and S. Granville, Exploring disorder in the spin gapless semiconductor Mn_2CoAl , *Mater. Res. Express* **6**, 106113 (2019).
- [59] H. Ehrenreich, H. R. Philipp, and B. Segall, Optical properties of aluminum, *Phys. Rev.* **132**, 1918 (1963).
- [60] C. C. Homes, M. Reedyk, D. A. Cradles, and T. Timusk, Technique for measuring the reflectance of irregular, submillimeter-sized samples, *Appl. Opt.* **32**, 2976 (1993).
- [61] A. B. Kuzmenko, Kramers–Kronig constrained variational analysis of optical spectra, *Rev. Sci. Instrum.* **76**, 083108 (2005).
- [62] B. P. P. Mallett, S. V. Chong, R. Guehne, A. Chan, P. Murmu, J. Kennedy, and R. G. Buckley, The electronic properties and defect chemistry of $\text{Bi}_{2-x}\text{Se}_3$, $-0.05 < x < 0.15$, *J. Phys. Chem. Solids* **148**, 109752 (2021).
- [63] P. Jernberg, S. Bjarman, and R. Wäppling, FePS_3 : A first-order phase transition in a “2D” Ising antiferromagnet, *J. Magn. Magn. Mater.* **46**, 178 (1984).
- [64] N. Chandrasekharan and S. Vasudevan, Dilution of a layered antiferromagnet: Magnetism in $\text{Mn}_x\text{Zn}_{1-x}\text{PS}_3$, *Phys. Rev. B* **54**, 14903 (1996).
- [65] Y. Takano, N. Arai, A. Arai, Y. Takahashi, K. Takase, and K. Sekizawa, Magnetic properties and specific heat of MPS_3 ($M = \text{Mn, Fe, Zn}$), *J. Magn. Magn. Mater.* **272–276**, E593 (2004).
- [66] J. Yang, Y. Zhou, Q. Guo, Y. Dedkov, and E. Voloshina, Electronic, magnetic and optical properties of MnPX_3 ($X = \text{S, Se}$) monolayers with and without chalcogen defects: A first-principles study, *RSC Adv.* **10**, 851 (2020).
- [67] C.-T. Kuo, M. Neumann, K. Balamurugan, H. J. Park, S. Kang, H. W. Shiu, J. H. Kang, B. H. Hong, M. Han, T. W. Noh *et al.*, Exfoliation and Raman spectroscopic fingerprint of few-layer NiPS_3 van der Waals crystals, *Sci. Rep.* **6**, 20904 (2016).
- [68] U. Fano, Effects of configuration interaction on intensities and phase shifts, *Phys. Rev.* **124**, 1866 (1961).
- [69] R. E. Dietz, G. I. Parisot, and A. E. Meixner, Infrared absorption and Raman scattering by two-magnon processes in NiO , *Phys. Rev. B* **4**, 2302 (1971).
- [70] J. Lorenzana and G. A. Sawatzky, Phonon assisted multi-magnon optical absorption and long lived two-magnon states in undoped lamellar copper oxides, *Phys. Rev. Lett.* **74**, 1867 (1995).
- [71] A. Damascelli, D. van der Marel, M. Grüninger, C. Presura, T. T. M. Palstra, J. Jegoudez, and A. Revcolevschi, Direct two-magnon optical absorption in $\alpha' - \text{NaV}_2\text{O}_5$: “Charged” magnons, *Phys. Rev. Lett.* **81**, 918 (1998).
- [72] <http://energy.gov/downloads/doe-public-access-plan>.